


## PAPER

[View Article Online](#)  
[View Journal](#) | [View Issue](#)Cite this: *Dalton Trans.*, 2024, **53**, 5484The role of reducibility *vis-à-vis* oxygen vacancies of doped  $\text{Co}_3\text{O}_4/\text{CeO}_2$  in the oxygen evolution reaction†Saraswati Roy,<sup>a</sup> Preeti Dahiya,<sup>b</sup> Tapas Kumar Mandal<sup>b,c</sup> and Sounak Roy  <sup>a,d</sup>

Electrochemical water splitting, which is a highly promising and environmentally friendly technology for  $\text{H}_2$  fuel production, faces significant hurdles due to the sluggish kinetics of the oxygen evolution reaction. Co-based oxides have garnered significant attention as alternative catalysts for the oxygen evolution reaction owing to the  $\text{Co}^{2+}/\text{Co}^{3+}$  redox couple. Enhancing the challenging  $\text{Co}^{2+} \rightarrow \text{Co}^{3+}$  oxidation process can further improve the catalytic oxygen evolution reaction. The aim of our work was to design a  $\text{Co}_3\text{O}_4$ -based catalyst to enhance reactivity by increasing the number of  $\text{Co}^{3+}$  active sites, serving as an excellent platform for facilitating the oxygen evolution reaction. To drive the effectiveness of the catalyst, in this study, we synthesized  $\text{Co}_3\text{O}_4$  anchored on  $\text{CeO}_2$  ( $\text{Co}_3\text{O}_4/\text{CeO}_2$ ). The kinetics and efficacy of the oxygen evolution reaction catalysed by  $\text{Co}_3\text{O}_4/\text{CeO}_2$  was significantly improved by aliovalent doping of Sr into Ce sites and Cu into Co sites. The reducible nature of Ce stimulates the formation of  $\text{Co}^{3+}$  ions, resulting in an increased production of intermediate  $-\text{OOH}$  species, thus expediting the reaction. The transformation of  $\text{Co}^{2+}$  to  $\text{Co}^{3+}$  consequently leads to an increase in anion vacancies, which, in turn, promotes the adsorption of more intermediate species at the active site. The Sr- and Cu-doped  $\text{Co}_3\text{O}_4/\text{CeO}_2$  catalyst exhibited a high current density of  $200 \text{ mA cm}^{-2}$  at 580 mV and a low overpotential of 297 mV at  $10 \text{ mA cm}^{-2}$ . The study functions as a key indicator to establish a connection between oxygen vacancies and metal oxidation states in order to investigate the mechanistic aspects of the oxygen evolution reaction on mixed metal oxides. Moreover, this study is expected to pave the way for the development of innovative oxygen evolution reaction catalysts with reducible supports, thus offering a new pathway for their design.

Received 1st February 2024,  
Accepted 15th February 2024

DOI: 10.1039/d4dt00315b

rsc.li/dalton

## 1. Introduction

The transient nature of the primary feedstock obtained from the spontaneous combustion of non-renewable fossil fuels has spurred the advancement of the sustainable  $\text{H}_2$  energy economy. Water electrolyzers enable the conversion of water into the energy carrier  $\text{H}_2$  through an electrochemical process. However, the bottleneck of this technology is the sluggish

anodic oxygen evolution reaction (OER) characterized by a four-electron transport process, the breaking of the O–H bond, and the subsequent formation of the O–O bond. These complex processes result in high kinetic energy barriers and, consequently, significant overpotentials.<sup>1,2</sup> In addition to water splitting, the OER is also a crucial half-reaction in processes such as  $\text{CO}_2$  and  $\text{N}_2$  electroreduction as well as in metal–air batteries. The practical implementation of common OER catalysts, such as Pt, Ru, and Ir, in large-scale applications is constrained by their high cost and limited availability. Therefore, extensive research is being conducted for developing affordable, stable, and efficient OER catalysts. In recent times, significant attention has been devoted to exploring non-noble metals as potential electrocatalysts for the OER.<sup>3–5</sup>

Among the transition metals, Co-based materials have garnered significant attention as alternative catalysts for the OER owing to their crucial redox couple, which promotes OER kinetics through surface reconstruction.<sup>6–8</sup> For instance, the bi-metallic hetero-structured hybrid nanorod  $\text{NiSe}_2\text{–CoSe}_2$  has been explored as an excellent OER catalyst.<sup>9</sup> Transitional metal

<sup>a</sup>Department of Chemistry, Birla Institute of Technology and Science Pilani, Hyderabad Campus, Hyderabad-500078, India.

E-mail: sounak.roy@hyderabad.bits-pilani.ac.in

<sup>b</sup>Department of Chemistry, Indian Institute of Technology Roorkee, Roorkee – 247 667, India<sup>c</sup>Centre for Nanotechnology, Indian Institute of Technology Roorkee, Roorkee – 247 667, India<sup>d</sup>Materials Center for Sustainable Energy & Environment, Birla Institute of Technology and Science Pilani, Hyderabad Campus, Hyderabad – 500078, India†Electronic supplementary information (ESI) available: The reliability factors along with refined lattice parameters of the catalysts,  $\text{N}_2$  adsorption isotherm, CV curves in the non-faradaic region at different scan rates, XPS, fluorescence and Raman spectra of the catalysts. See DOI: <https://doi.org/10.1039/d4dt00315b>

boride-based materials are well-known catalysts for the water-splitting reaction.<sup>10</sup> Based on the literature, it is widely believed that during the OER, the first redox feature of the  $\text{Co}^{2+}/\text{Co}^{3+}$  couple facilitates the formation of essential  $\text{Co}^{3+}$ -OOH species under basic conditions, while the second redox feature of the  $\text{Co}^{3+}/\text{Co}^{4+}$  couple promotes the formation of  $\text{Co}^{4+}\text{O}_2$ .<sup>11,12</sup> In our earlier report, we have exclusively shown that  $\text{Co}^{2+}/\text{Co}^{3+}$  oxidation in  $\text{Co}_3\text{O}_4$  aids the facile occurrence of the OER.<sup>13</sup> However, the oxidation of Co to its highest possible oxidation state *i.e.*  $\text{Co}^{2+}/\text{Co}^{3+}$  and  $\text{Co}^{3+}/\text{Co}^{4+}$  must occur alongside parallel reduction reactions, which require a support material with facile reducibility.

To create an efficient  $\text{Co}^{2+}/\text{Co}^{3+}$  and  $\text{Co}^{3+}/\text{Co}^{4+}$  redox system in  $\text{Co}_3\text{O}_4$ , in this work, we have developed cerium-dioxide-supported cobalt oxide ( $\text{Co}_3\text{O}_4/\text{CeO}_2$ ) by a solution combustion method.  $\text{CeO}_2$  can improve the electrical conductivity and optical activity of  $\text{Co}_3\text{O}_4$  as the oxidation of cobalt is facilitated by the reduction of cerium and/or lattice oxygen evolution ( $\text{O}^{2-} \rightarrow \frac{1}{2}\text{O}_2 + 2\text{e}^-$ ).<sup>14</sup> The ability of  $\text{CeO}_2$  to transit between the  $\text{Ce}^{3+}$  and  $\text{Ce}^{4+}$  oxidation states allows it to facilitate reversible surface oxygen ion exchange. This property serves as an oxygen buffer for effective oxygen supply and also creates the potential for robust electron interactions with other materials.<sup>15</sup> Moreover, density functional theory calculations suggest that  $\text{CeO}_x$  can influence the electronic properties of cobalt species.<sup>16,17</sup> We further substituted Ce with Sr ( $\text{Co}_3\text{O}_4/\text{Ce}_{1-y}\text{Sr}_y\text{O}_{2-\delta}$ ) to enhance the oxidizing power of  $\text{CeO}_2$  as Sr with a lower oxidation potential is a judicious choice for ameliorating the redox behaviour of cerium and cobalt.<sup>18–23</sup> To further enhance the impact of oxygen vacancies, we partially substituted the cobalt sites with another transition metal, namely Cu ( $\text{Co}_{3-x}\text{Cu}_x\text{O}_4/\text{Ce}_{1-y}\text{Sr}_y\text{O}_{2-\delta}$ ). The substitution of cobalt with copper will elevate the oxidation state of cobalt. In addition, it can also accelerate the formation of oxygen vacancies to maintain the charge balance.<sup>24,25</sup> The study shows the crucial roles of the reducible  $\text{CeO}_2$  support and  $\text{Cu}^{2+}$  doping in  $\text{Co}_3\text{O}_4$  in facilitating the oxidation of  $\text{Co}^{2+}/\text{Co}^{3+}$  and  $\text{Co}^{3+}/\text{Co}^{4+}$  and their impact on the catalytic oxygen evolution reaction.

## 2. Experimental methods

The  $\text{Co}_3\text{O}_4/\text{CeO}_2$  catalysts were synthesized using a novel solution combustion method, which is known for its energy efficiency and low-temperature initiation.<sup>13</sup> During synthesis, water-soluble  $\text{Ce}(\text{NO}_3)_3 \cdot 6\text{H}_2\text{O}$  (SRL chemicals, 99%),  $\text{Co}(\text{NO}_3)_2 \cdot 6\text{H}_2\text{O}$  (S.D. Fine Chem Limited, 99%),  $\text{Sr}(\text{NO}_3)_2$  (Sigma Aldrich, 99%), and  $\text{Cu}(\text{NO}_3)_2 \cdot 6\text{H}_2\text{O}$  (S.D. Fine Chem Limited, 99%) were utilized as oxidizers, while glycine served as the fuel. The synthesis of 40%  $\text{Co}_3\text{O}_4/\text{CeO}_2$  was carried out by dissolving 0.58 g of  $\text{Co}(\text{NO}_3)_2 \cdot 6\text{H}_2\text{O}$ , 0.87 g of  $\text{Ce}(\text{NO}_3)_3 \cdot 6\text{H}_2\text{O}$ , and 0.2 g of glycine in 50 mL of water. The resulting homogeneous aqueous solution was then placed in a preheated furnace at 450 °C for 15 minutes. Initially, the solution exhibited boiling and foaming; the exothermic redox reaction generated

sufficient heat of combustion, compensating for the energy required for oxide formation and resulting in a burning flame at the ignition point. Subsequently, the complete dehydration of the solution yielded the solid powder product of pristine  $\text{Co}_3\text{O}_4/\text{CeO}_2$ , accompanied by the evolution of  $\text{N}_2$  and  $\text{CO}_2$ . Henceforth,  $\text{Co}_3\text{O}_4/\text{CeO}_2$  is denoted as CoCe in the manuscript. About 0.58 g of  $\text{Co}(\text{NO}_3)_2 \cdot 6\text{H}_2\text{O}$ , 0.34 g of  $\text{Ce}(\text{NO}_3)_3 \cdot 6\text{H}_2\text{O}$ , 0.04 g of  $\text{Sr}(\text{NO}_3)_2$  and 0.29 g of glycine were used for the synthesis of 40%  $\text{Co}_3\text{O}_4/\text{Ce}_{0.9}\text{Sr}_{0.1}\text{O}_{2-\delta}$  (designated as CoSrCe) and 0.78 g of  $\text{Co}(\text{NO}_3)_2$ , 0.08 g of  $\text{Cu}(\text{NO}_3)_2 \cdot 6\text{H}_2\text{O}$ , 0.34 g of  $\text{Ce}(\text{NO}_3)_3 \cdot 6\text{H}_2\text{O}$ , 0.04 g of  $\text{Sr}(\text{NO}_3)_2$  and 0.37 g of glycine were used to synthesise 40%  $\text{Co}_{3-x}\text{Cu}_x\text{O}_4/\text{Ce}_{0.9}\text{Sr}_{0.1}\text{O}_{2-\delta}$  (designated as CoCuSrCe) in a similar manner.

The structure and crystallinity of the prepared mixed metal oxides were characterized using X-ray diffraction (XRD) data obtained using a Rigaku Ultima IV instrument with  $\text{Cu K}\alpha$  radiation. The XRD scans were performed at a scan rate of  $0.02^\circ \text{ min}^{-1}$  with a step size of  $0.01^\circ$ . The nanocrystalline size of the synthesized metal was determined using Debye-Scherrer's formula ( $D = 0.9\lambda/B \cos \theta$ ), where  $\lambda$  is the wavelength of the radiation,  $B$  is the full-width at half-maximum, and  $\theta$  is the corresponding angle. The surface morphology and composition analyses were conducted using a Field Emission Scanning Electron Microscope (FE-SEM, FEI-Apereo S) equipped with an Energy Dispersive X-ray Spectroscopy (EDX) unit. The instrument was operated at an acceleration voltage of 20 kV. The Brunauer-Emmett-Teller (BET) method was employed to determine the surface area and pore size of the synthesized catalysts. The X-ray photoelectron spectra (XPS) of the synthesized catalysts were recorded using a Thermo Scientific K-Alpha surface analysis spectrometer with  $\text{Al K}\alpha$  radiation (1486.6 eV). The binding energies were reported with respect to C (1s) at 284.8 eV. The EPR analysis was conducted using a Bruker ESR 5000. A UniRam Raman spectroscopy system was used for Raman spectroscopy.

The electrochemical tests of the synthesized materials were conducted using a conventional three-electrode system. The working electrode was prepared by coating the synthesized catalyst onto Ni foam (NF). The reference electrode used was  $\text{Hg}/\text{HgO}$  saturated with an aqueous KOH solution, and a Pt wire served as the counter electrode. For the preparation of the working electrode, 3 mg of the synthesized catalyst and 0.5 mg of carbon black powder were dispersed in 1 mL of methanol. Additionally, 10  $\mu\text{L}$  of 5% aqueous Nafion (Sigma-Aldrich) was added to the solution. The mixture was sonicated for 60 minutes to achieve a homogenized dispersion of the synthesized metal oxides and carbon. The active mass ratio of the catalyst to carbon black was maintained at 6 : 1.5. The NF electrode was cut into pieces of  $1 \times 0.3 \text{ cm}^2$  and soaked in 0.3 M  $\text{H}_2\text{SO}_4$  for 15 minutes. It was then ultrasonically washed with acetone followed by distilled water. An ink prepared with 50  $\mu\text{L}$  of the catalyst was drop-casted onto the clean NF electrode, with an active mass loading of  $0.1 \text{ mg cm}^{-2}$ . The electrode was left to dry at room temperature. Cyclic voltammetry (CV), linear sweep voltammetry (LSV), and electrochemical impedance spectroscopy (EIS) measurements were performed in a



basic electrolyte medium of 1 M KOH using a scan rate of 10 mV s<sup>-1</sup>. The CV cycles and OER polarization curves from LSV traces were recorded between 0.9 and 1.9 V (vs. RHE). The obtained potentials were converted to values corresponding to the reversible hydrogen electrode (RHE) using the equation:  $E_{\text{RHE}} = E_{\text{Hg/HgO}} + 0.059\text{pH} + E_{\text{Hg/HgO}}^{\circ}$ . Here,  $E_{\text{RHE}}$  represents the final converted potential with respect to RHE,  $E_{\text{Hg/HgO}}$  is the experimental potential with respect to the Hg/HgO electrode, and  $E_{\text{Hg/HgO}}^{\circ}$  is the standard reduction potential of the Hg/HgO electrode. To evaluate material stability, chronoamperometric (CA) measurements were performed in a three-electrode system for 12 hours in 1 M KOH. EIS was carried out in the frequency range of 100 kHz to 10 mHz, by applying the overpotential versus Hg/HgO. The gaseous product O<sub>2</sub> was measured using a portable Gas Chromatograph (GC) from Mayura Analytical Pvt. Limited, India.

### 3. Results and discussion

#### 3.1 Structure and surface of the catalysts

The XRD patterns and the refinements of the synthesized composite metal oxides are shown in Fig. 1(a–c). The Rietveld refinements were carried out by using the Fullprof program suite. The diffraction patterns of all the synthesized catalysts exhibited sharp peaks, indicating high crystallinity, and based on the Debye–Scherrer formula, the crystallite sizes were found to be ~30 nm for all the materials. From Fig. 1a, it is evident that crystals of both Co<sub>3</sub>O<sub>4</sub> with space group *Fd3m* (S.G. no. 227, JCPDS #43-1003) and CeO<sub>2</sub> with space group *Fm3m* (S.G. no. 225, JCPDS #34-0394) were clearly present in CoCe. Similarly, the Rietveld refinement of the diffraction data of CoSrCe confirmed the coexistence of Co<sub>3</sub>O<sub>4</sub> and Sr-doped CeO<sub>2</sub> (Fig. 1b). On the other hand, the CoCuSrCe data in Fig. 1c exhibit the presence of four phases, namely, Sr-doped CeO<sub>2</sub> with space group *Fm3m* (S.G. no. 225, JCPDS #34-0394), Cu-doped Co<sub>3</sub>O<sub>4</sub> with space group *Fd3m* (S.G. no. 227, JCPDS #43-1003), tetragonal SrCoO<sub>2.8</sub> with space group *I4/mmm* (S.G. no. 139, JCPDS #39-1084) and monoclinic CuO with space group *C2/c* (S.G. no. 15, JCPDS #05-0661). The Rietveld refinement of the compound, incorporating mixed phases, has successfully achieved a well-fitting profile for the data. The reliability factors along with the refined lattice parameters and constraints of all the phases from the three synthesized composite catalysts are provided in Tables S1–S3.† Elemental doping was corroborated by the XRF studies, as shown in Table S4.†

As electrocatalysis is a surface phenomenon, next, we studied the surface properties of the combustion-synthesized materials. The FESEM micrographs in the insets of Fig. 1(a–c) show the surface morphologies of pristine CoCe, doped CoSrCe and CoCuSrCe. All three materials showed a similar spherical particle morphology with an average diameter of ~0.17 μm. EDX elemental mapping indicated the surface enrichment of dopants Cu and Sr in the matrix (Fig. 1(d–f) and Table S4†). This was further verified by the other spot EDX elemental mappings shown in Fig. S1.† The surface area was

also studied, and all the materials exhibited type II N<sub>2</sub> adsorption–desorption isotherms with negligible hysteresis, specifying the nanoporous nature of the surface (Fig. S2†). The average surface areas of the materials estimated using the BET equation were found to be in the 1–3 m<sup>2</sup> g<sup>-1</sup> range.

The electrochemical active surface area (ECSA) plays an important role in the electrocatalytic activity of a material. The ECSA was calculated from the electrochemical double layer capacitance ( $C_{\text{dl}}$ ) and specific capacitance ( $C_{\text{s}}$ ) according to the equation:  $\text{ECSA} = C_{\text{dl}}/C_{\text{s}}$ .<sup>26,27</sup> The  $C_{\text{dl}}$  values were obtained from the CV curves obtained in the non-faradaic region (0.72 to 1.32 V vs. RHE) in 1 M KOH at various scan rates (10–50 mV s<sup>-1</sup>), as shown in Fig. S3.† The current is linearly proportional to the active surface area owing to the charging of the double layer, and the slope obtained from the plot of half of the capacitive current ( $\Delta j/2 = (j_{\text{anodic}} - j_{\text{cathodic}})/2$ ) against the scan rate is defined as  $C_{\text{dl}}$ .<sup>28</sup> The representative  $C_{\text{dl}}$  values of the synthesized materials were obtained from the curves presented in Fig. 2a. The  $C_{\text{s}}$  was calculated using the following equation:

$C_{\text{s}} = \frac{\int v dv}{m \times V_{\text{s}} \times \Delta V}$ , where  $\int v dv$  (mA mV) is the area under the CV curve cycled at the scan rate of 10 mV s<sup>-1</sup>,  $m$  (0.1 mg) is the active mass of the catalyst loaded on the electrode (area = 0.6 cm<sup>2</sup>),  $V_{\text{s}}$  is the scan rate (mV s<sup>-1</sup>) and  $\Delta V$  is the potential window (mV). Thus, the obtained  $C_{\text{s}}$  values with respect to unit mass loading (mF mg<sup>-1</sup>) were converted to mF cm<sup>-2</sup>. The representative ECSAs were found to be 2.36, 5.7 and 6.9 cm<sup>2</sup> for CoCe, CoSrCe and CoCuSrCe, respectively (Fig. 2b). An apparent 3-fold increase in electrochemical surface area was observed with the concomitant doping of Sr and Cu in CoCe.

XPS was used to probe the surface elemental composition and oxidation states of the synthesized catalysts. The survey spectra of all the synthesized catalysts displayed the expected elements (Fig. S4a†). The areas under the peaks of the corresponding elements were derived using the peak fitting software Avantage, and the values were normalized against the X-ray energy used. The surface atomic percentages were calculated by dividing the normalized peak area by the respective photoionization cross-section of the corresponding elements.<sup>29</sup> Table S4† indicates surface enrichment of Sr and Cu than the bulk. The deconvoluted Ce 3d core level spectra (3d<sub>5/2</sub> is labelled as v, and 3d<sub>3/2</sub> is labelled as u) of CoCe, CoSrCe, and CoCuSrCe are presented in Fig. 3a. The spectra exhibited a total of 5 spin–orbit coupled peaks, of which v–u, v'–u', and v''–u''' belong to Ce<sup>4+</sup>, and v<sub>o</sub>–u<sub>o</sub> and v'–u' belong to Ce<sup>3+</sup>. The Ce<sup>4+</sup> doublets designated as v–u (882.2–901.0 eV), v'–u' (889.3–907.3 eV) and v''–u''' (897.0–916.5 eV) are associated with the Ce 3d<sup>9</sup>4f<sup>2</sup>O 2p<sup>4</sup>, Ce 3d<sup>9</sup>4f<sup>1</sup>O 2p<sup>5</sup> and Ce 3d<sup>9</sup>4f<sup>0</sup>O 2p<sup>6</sup> final states, respectively. The other two doublets of Ce<sup>3+</sup> positioned at v<sub>o</sub>–u<sub>o</sub> (879.6–898.5 eV) and v'–u' (885.3–903.0) correspond with the Ce 3d<sup>9</sup>4f<sup>2</sup>O 2p<sup>5</sup> and Ce 3d<sup>9</sup>4f<sup>1</sup>O 2p<sup>6</sup> final states.<sup>30–32</sup> The relative surface concentrations ( $C$ ) of Ce<sup>3+</sup> and Ce<sup>4+</sup> were estimated from the total area under the deconvoluted peak ( $A$ ) by using the following equations:

$$A_{\text{Ce}^{3+}} = A_{v_o} + A_{u_o} + A_{v'} + A_{u'}$$





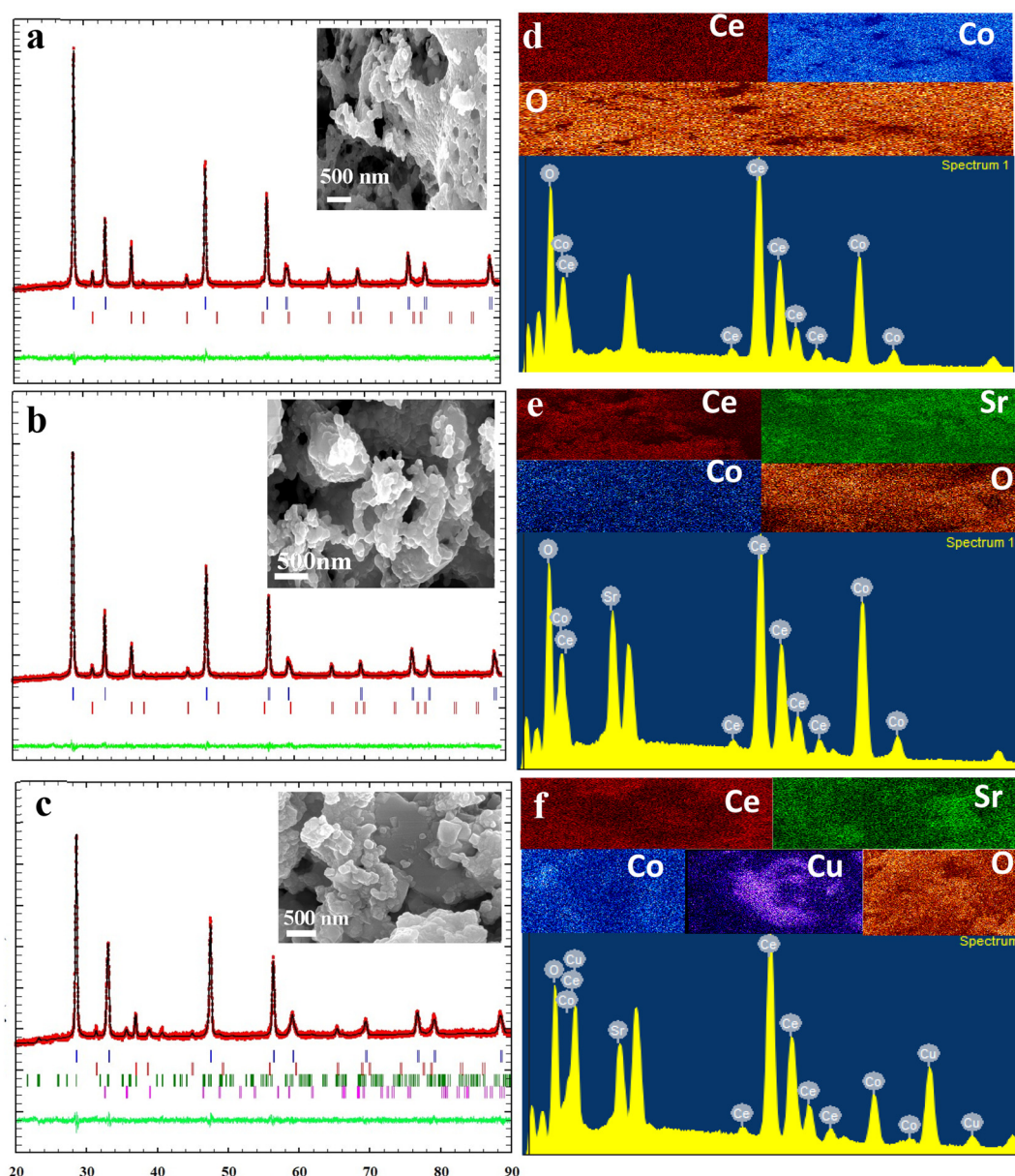


**Fig. 1** Rietveld refinement profiles of (a) CoCe, (b) CoSrCe and (c) CoCuSrCe. The blue vertical lines represent the Bragg positions of CeO<sub>2</sub> and Sr-doped CeO<sub>2</sub> fluorite phases, and the red lines indicate those of the Co<sub>3</sub>O<sub>4</sub> and Cu-doped Co<sub>3</sub>O<sub>4</sub> spinel phases. The green vertical lines represent the Bragg positions of SrCoO<sub>2.8</sub>, and the pink lines represent those of CuO. The corresponding FESEM images are provided as insets. The EDX mappings and elemental analysis of (d) CoCe, (e) CoSrCe and (f) CoCuSrCe.

$$A_{\text{Ce}^{4+}} = A_v + A_u + A_v'' + A_u'' + A_v''' + A_u'''$$

$$C_{\text{Ce}^{4+}} = A_{\text{Ce}^{4+}} / (A_{\text{Ce}^{4+}} + A_{\text{Ce}^{3+}}) \times 100\%$$

According to the calculations, the percentage of Ce<sup>4+</sup> present in CoCe, CoSrCe, and CoCuSrCe were 65.6, 68.0 and 74.1%, respectively. Apparently, the occurrence of Ce<sup>4+</sup> increased with Sr and Cu doping. Fig. 3b exhibits the high-resolution Co 2p core level spin-orbit doublet peaks of the three catalysts, which demonstrate the 2p<sub>3/2</sub> and 2p<sub>1/2</sub> peaks

associated with the Co<sup>2+</sup> and Co<sup>3+</sup> ions. The Co<sup>2+</sup> peak appeared at a higher binding energy (2p<sub>3/2</sub>-2p<sub>1/2</sub> at 782.5–796.2 eV) than the Co<sup>3+</sup> peak (2p<sub>3/2</sub>-2p<sub>1/2</sub> at 780.0–795 eV).<sup>13,33</sup> The percentage of Co<sup>3+</sup> present in CoCe, CoSrCe, and CoCuSrCe were 61.02, 67.9, and 71.1%, respectively. It is interesting to observe that with the incorporation of lower valent Sr and Cu at the Ce and Co sites, respectively, the Ce and Co ions underwent oxidation for charge neutralization. We also collected the core-level Cu 2p spectrum of CoCuSrCe (Fig. 3c), which showed the presence of bivalent Cu<sup>2+</sup> with the peaks of Cu 2p<sub>3/2</sub> and Cu 2p<sub>1/2</sub> associated with the Cu<sup>2+</sup> and Cu<sup>1+</sup> ions



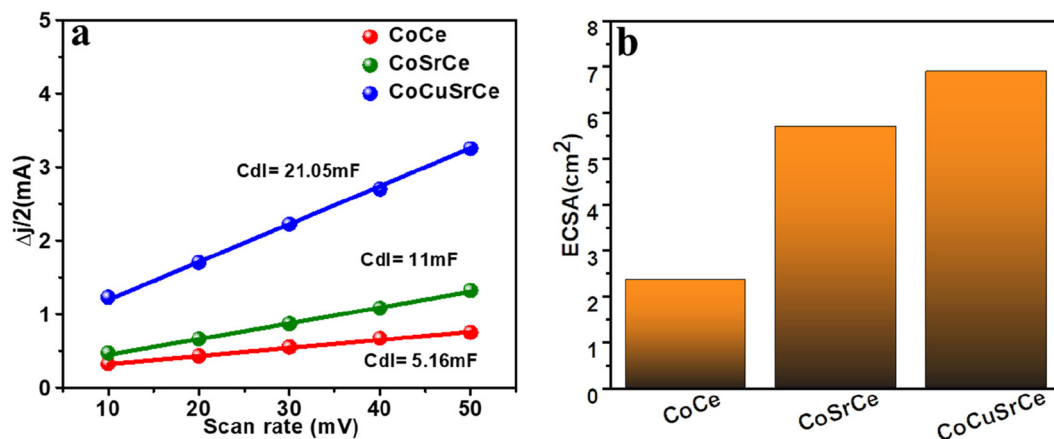


Fig. 2 (a) Linear regression between current density differences vs. scan rates based on CV in a potential window of 1.16 V, and (b) ECSAs of the three composite catalysts.

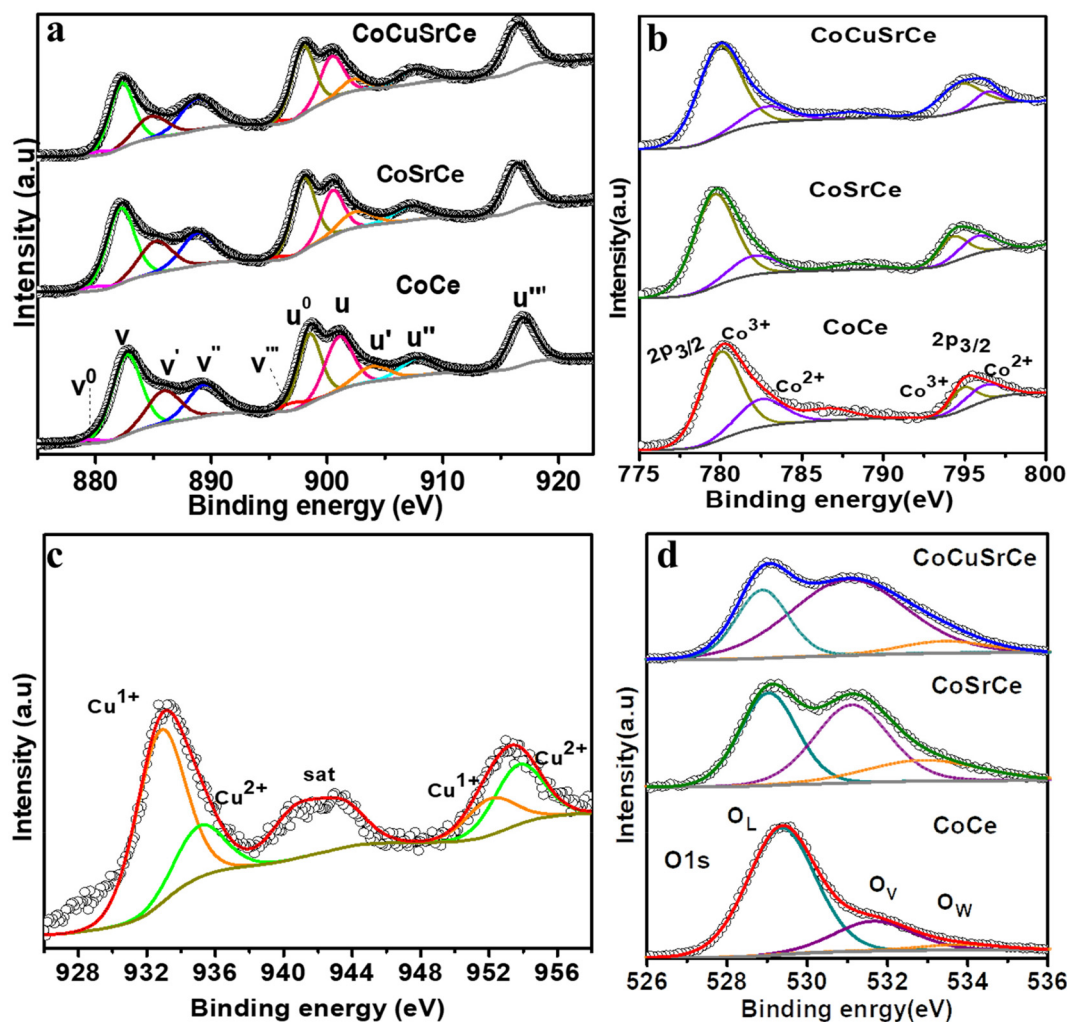


Fig. 3 (a) The Ce 3d core level spectra, (b) Co 2p core level spectra, (c) Cu 2p core level spectra, and (d) O 1s core level spectra of the synthesized pristine and doped oxides.



at 933.5 and 953.3 eV, respectively.<sup>32,34–38</sup> The Cu<sup>2+</sup> peak appeared at a higher binding energy (2p<sub>3/2</sub>–2p<sub>1/2</sub> at 934.9–954.7 eV) than the Cu<sup>1+</sup> peak (2p<sub>3/2</sub>–2p<sub>1/2</sub> at 933–952.8 eV).<sup>39</sup> The Cu L<sub>3</sub>M<sub>45</sub>M<sub>45</sub> Auger spectrum in Fig. S4b† distinctively shows the Cu<sup>1+</sup> peaks at 916 eV and Cu<sup>2+</sup> at 917 eV. The percentage of Cu<sup>2+</sup> present in CoCuSrCe was found to be 50.29%. We also checked the Cu 2p core level spectrum of CoCuSrCe after the OER study (Fig. S4c†). The XPS data revealed that lattice doping with lower-valent elements, such as Sr<sup>2+</sup> and Cu<sup>2+</sup>, induced further oxidation of Ce and Co. This phenomenon suggests the potential creation of oxygen vacancies as well. Therefore, a detailed XPS study of O 1s was performed for all three catalysts, and the deconvoluted spectra are plotted in Fig. 3d. The spectra showed three distinct peaks: one at 529 eV due to lattice oxygen (O<sub>L</sub>), one at 531 eV due to the adsorbed oxygen species at the surface defect sites *i.e.* oxygen vacancies (O<sub>V</sub>), and one at 533 eV due to the hydroxyl species of the surface-adsorbed water molecules (O<sub>W</sub>). The percentage of surface oxygen vacancies in each catalyst was quantified from the area under the O<sub>V</sub> peak with respect to the total area under the O 1s core level spectrum (O<sub>T</sub>)<sup>40–43</sup> with the help of the following equation:

$$O_V(\%) = \frac{O_V}{O_T} \times 100\%, \quad \text{where } O_T = O_V + O_L + O_W.$$

The percentage of oxygen vacancies was found to be 27% in pristine CoCe. Interestingly, the O<sub>V</sub> content (%) increased to 65 and 74% in CoSrCe and CoCuSrCe, respectively. The O<sub>L</sub> content (%) in the materials was also calculated in a similar manner, and the values were found to be 69.3, 36.2 and 21.8% for CoCe, CoSrCe, and CoCuSrCe, respectively. Apparently, lattice doping of bivalent Sr<sup>2+</sup> and Cu<sup>2+</sup> not only made Ce and Co undergo further oxidation but also created sufficient surface oxygen vacancies. Surface oxygen vacancies are known to facilitate the formation of the –OOH species, a key OER intermediate.

A correlation between the occurrence of oxygen vacancies and doping was also established using the fluorescence spectra. Fig. S5a† illustrates a gradual decrease in fluorescence intensity with Sr and Cu doping, indicating that the absorbed light is trapped by oxygen vacancies (O<sub>V</sub>). Among the three oxides, CoCuSrCe exhibited the lowest intensity, suggesting the formation of oxygen vacancies.<sup>42</sup> To further confirm the presence of O<sub>V</sub>, we conducted Raman spectroscopy. Fig. S5b† shows that the Raman peak intensity at 548 cm<sup>–1</sup> corresponding to O<sub>V</sub> (A<sub>1g</sub> mode)<sup>41</sup> increased in the order of CoCe < CoSrCe < CoCuSrCe, indicating an increase in the formation of oxygen vacancies with doping. The yellow-highlighted region in the range of 440–460 cm<sup>–1</sup> in the Raman spectra indicates the presence of Co–O and Ce–O bonds.<sup>44,45</sup>

### 3.2 OER

The catalytic OER activity of the synthesized materials deposited on Ni foam electrodes was measured in 1 M KOH using LSV polarization curves, as shown in Fig. 4a. For clarity, the activity of the bare Ni foam electrode is also plotted in the graph. The three catalysts exhibited a prominent peak at ~1.4

V vs. RHE before the OER onset potential. This peak can be attributed to the oxidation of Co<sup>2+</sup> to Co<sup>3+</sup>.<sup>46</sup> Interestingly, from the peak current density, it was observed that the extent of Co oxidation increased with Sr doping at the Ce sites and consequently Cu doping at the Co sites. Notably, the highly oxidized Co<sup>3+</sup> facilitates the formation of the key OER intermediate species –OOH. Fig. 4a represents that compared to pristine CoCe, CoSrCe exhibited a lower onset potential, as well as a lower OER overpotential. Among the three catalysts, CoCuSrCe displayed the lowest overpotential. The higher extent of Co<sup>2+</sup> → Co<sup>3+</sup> oxidation, which leads to the formation of the intermediate –OOH species with the help of oxygen vacancies (as observed from the XPS studies), is apparently proportional to the OER catalytic activity of pristine and doped oxides. For benchmarking, a commercial RuO<sub>2</sub> sample was measured under similar conditions, and the oxides clearly outperformed the commercial RuO<sub>2</sub> catalyst. The overpotential required to achieve a current density of 10 mA cm<sup>–2</sup> is a widely accepted metric for solar fuel production. Hence, the overpotentials at 10, 50 and 100 mA cm<sup>–2</sup> were plotted for the synthesized materials, as shown in Fig. 4b. Fig. 4b demonstrates that the best OER activities of CoCuSrCe with the lowest overpotential were 297, 410 and 470 mV at 10, 50 and 100 mA cm<sup>–2</sup>, respectively. We further compared the OER activity data with other reported Co-based catalysts, and Table 1 demonstrates that CoCuSrCe exhibits comparable or even superior performance to the other Co-based catalysts. For a global comparison and practical applicability, good mass activity, as well as intrinsic activity, of a catalyst is highly desirable. The mass activity of electrochemical OER catalysts is determined by normalizing the current density to the loaded amount of catalyst, whereas, the intrinsic activity is the current density per unit electrochemical active surface area. Fig. 4c shows the mass activity and intrinsic activity of the three catalysts at the OER onset potential. Evidently, CoCuSrCe exhibited a far superior OER catalytic activity to the pristine and only Sr-doped oxides. To corroborate the superiority of CoCuSrCe, we further measured the oxygen evolved during OER with the help of gas chromatography, and thereby calculated the faradaic efficiency using the following equation:

$$\begin{aligned} \text{FE}_{\text{O}_2} \% &= \frac{\text{Experimentally produced O}_2}{\text{Theoretically calculated O}_2} \times 100\% \\ &= \frac{\text{mol of O}_2 \times n \times F}{i \times t} \times 100\% \end{aligned}$$

where *n* is the total number of electrons transferred, *F* is the Faraday constant, *i* is the amount of current produced and *t* denotes time. The calculated FE<sub>O<sub>2</sub></sub> % values are plotted in Fig. 4d. Apparently, the FE<sub>O<sub>2</sub></sub> % of CoCuSrCe (84%) turned out to be better than those of the other two catalysts.

To understand the kinetics of the OER over the three synthesized catalysts, the scan rate dependency of their OER activity and the activation energy of the OER were evaluated. Scan rate dependency studies were carried out by varying the scan rate from 10 to 50 mV s<sup>–1</sup> in the presence of 1 M KOH as the electrolyte. Fig. 5a unveils that the OER current density lin-





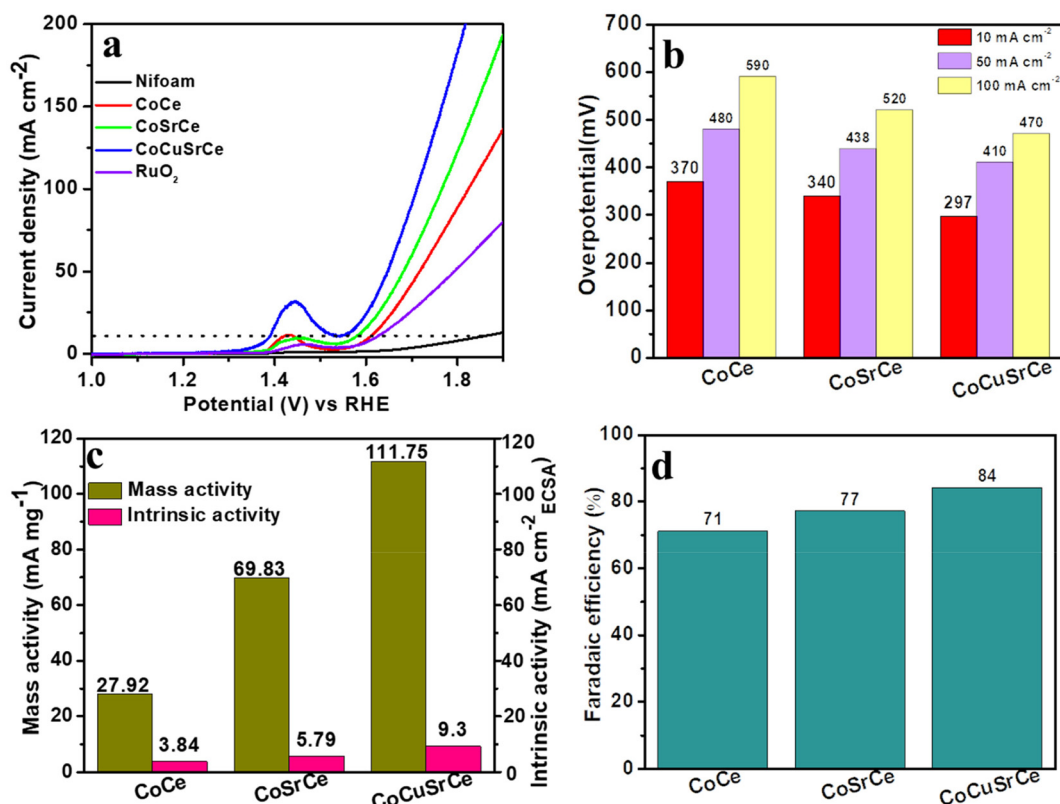


**Fig. 4** (a) OER polarisation curves of the three catalysts synthesized with bare Ni foam and the commercial RuO<sub>2</sub> catalyst; (b) overpotentials, (c) mass activity and intrinsic activity, and (d) FE (%) of oxygen evolution of the synthesized materials.

**Table 1** Comparison of OER activity data of pristine and supported Co<sub>3</sub>O<sub>4</sub> catalysts with previous works

Catalysts	Measurement conditions	OER activity		Ref.
		Overpotential at 10 mA cm <sup>-2</sup>	Tafel slope	
Co <sub>3</sub> O <sub>4</sub> nanoarrays on carbon	0.1 M KOH	0.29 V	70 mV dec <sup>-1</sup>	47
Co <sub>3</sub> O <sub>4</sub> nanoparticles	1 M KOH with 5 mV s <sup>-1</sup> scan rate	0.38 V	153 mV dec <sup>-1</sup>	48
Co <sub>3</sub> O <sub>4</sub> -ZIF 8	1 M KOH with 10 mV s <sup>-1</sup> scan rate	0.40 V	82 mV dec <sup>-1</sup>	49
Co(OH) <sub>2</sub> on GC	1 M NaOH with 10 mV s <sup>-1</sup> scan rate	0.4 V	90 mV dec <sup>-1</sup>	50
Co <sub>3</sub> O <sub>4</sub> nanocubes	1 M KOH with 1 mV s <sup>-1</sup> scan rate	0.5 V	59 mV dec <sup>-1</sup>	51
Co <sub>3</sub> O <sub>4</sub> @CoO	0.5 M KOH	0.43 V	89 mV dec <sup>-1</sup>	52
CoO <sub>x</sub> /CeO <sub>x</sub>	1 M NaOH with 10 mV s <sup>-1</sup> scan rate	0.31 V	66 mV dec <sup>-1</sup>	17
Co <sub>3</sub> O <sub>4</sub> /CeO <sub>2</sub> nanohybrids (NHs)	1 M NaOH with 10 mV s <sup>-1</sup> scan rate	0.27 V	60 mV dec <sup>-1</sup>	14
Co <sub>3</sub> O <sub>4</sub> /CeO <sub>2</sub> heterojunction	1 M KOH	0.25 V <sup>a</sup>	34.4 mV dec <sup>-1</sup>	53
CoCuSrCe	1 M KOH	0.29 V	42 mV dec <sup>-1</sup>	This work

<sup>a</sup> At 100 mA cm<sup>-2</sup>.

early increased with the square root of the scan rate, indicating a diffusion-controlled electrocatalytic reaction over these catalysts.<sup>54</sup> The Arrhenius plots of CoCe, CoSrCe, and CoCuSrCe showing current density ( $\ln j$ ) vs. temperature ( $T^{-1}$ ) at the OER potential were charted to determine the activation energy. The temperature was varied from 25 to 50 °C with a gap of 5 °C. The activation energy ( $E_a$ ) was obtained from the slope values in Fig. 5b. The activation energy of pristine CoCe was 14.8 kJ mol<sup>-1</sup>, whereas CoSrCe and CoCuSrCe exhibited activation

energies of 12.3 and 11.7 kJ mol<sup>-1</sup>, respectively. The lower activation energy indicates faster OER kinetics over CoCuSrCe.

A good electrocatalyst with considerable charge transfer ability should have a low Tafel slope. Fig. 6a shows the lowest Tafel slope of 42 mV dec<sup>-1</sup> for CoCuSrCe compared with 78 mV dec<sup>-1</sup> over pristine CoCe. The low Tafel slope indicates an improved charge transfer between the doped electrode material and the electrolyte, rationalizing its efficient OER activity. The Nyquist impedance plots (Fig. 6b) also supported



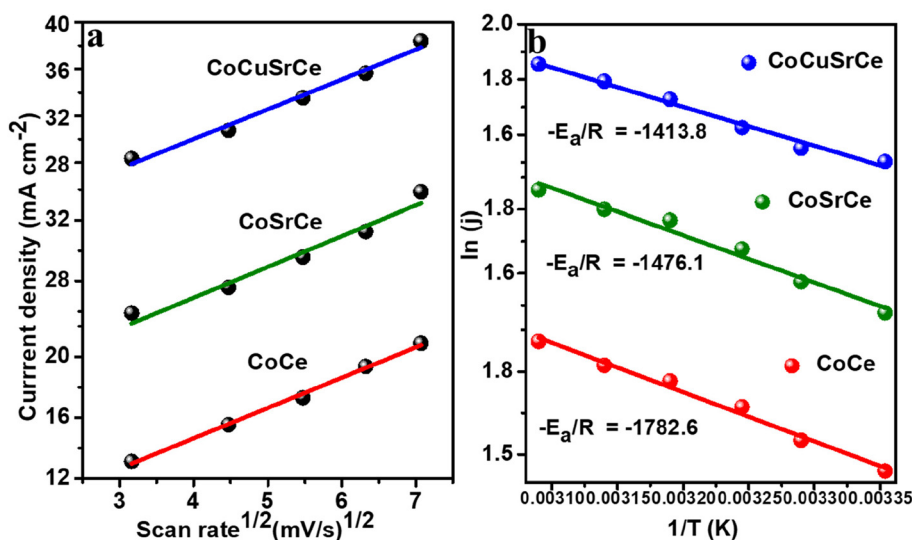


Fig. 5 (a) Scan rate dependency study and (b) activation energy plots of the oxygen evolution reactions over the synthesized materials.

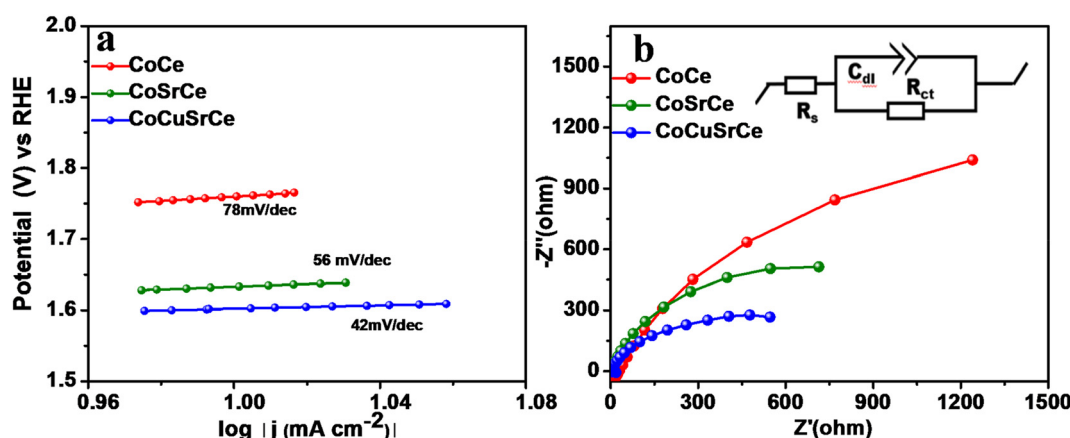


Fig. 6 (a) Tafel plots and (b) Nyquist plots of the three composite catalysts.

the OER efficacy trend of the materials. EIS measurements were performed under OER conditions (1 M KOH), and the data were fitted to the equivalent circuit shown in the inset of Fig. 6b. The equivalent circuit revealed one polarisation resistance ( $R_{ct}$ ) with a parallel constant-phase resistance. CoCuSrCe showed a smaller semicircle than those of CoSrCe and CoCe, suggesting faster shuttling of charges due to higher conductivity in the double-doped composite catalyst.<sup>55,56</sup>

The electrochemical stability of the best catalyst was evaluated by chronoamperometry studies in a 1 M KOH solution for 22 h at the corresponding OER overpotential. A remarkably stable OER current density was observed with CoCuSrCe (Fig. 7). To corroborate this further, we also collected the LSV traces of CoCuSrCe before and after the 22 h chronoamperometry study. The inset in Fig. 7 demonstrates the almost identical current densities of the fresh and exhausted catalysts, signifying the outstanding stability of the catalyst even at a considerably strong alkaline condition.

### 3.3 Mechanism

The superiority of the OER catalytic activity of double-doped CoCuSrCe intrigued us to probe the mechanism of the reaction in the presence of this material. In order to understand the role of the doped oxides, we thoroughly characterized the exhausted CoCuSrCe catalyst after 12 h of OER chronoamperometry. Fig. 8a shows the XRD pattern of the exhausted material along with the FESEM image in the inset. While the bulk crystalline structure remained unchanged, some minor additional peaks at  $2\theta = 35.4^\circ$ ,  $39.06^\circ$  and  $40.9^\circ$  were observed. These peaks correspond to the crystalline structures of  $\text{Co(OH)}_2$ ,  $\text{Cu(OH)}_2$  and  $\text{Co-OOH}$  formed during the OER.<sup>57–59</sup> The crystalline peaks of  $\text{M(OH)}_2$  confirm the active involvement of Co and Cu in the OER reaction mechanism. The formation of  $\text{M(OH)}_2$  and their apparent oxidation to form  $\text{M-OOH}$  species evidently modifies the surface morphology of the exhausted CoCuSrCe, as observed in the FESEM image.





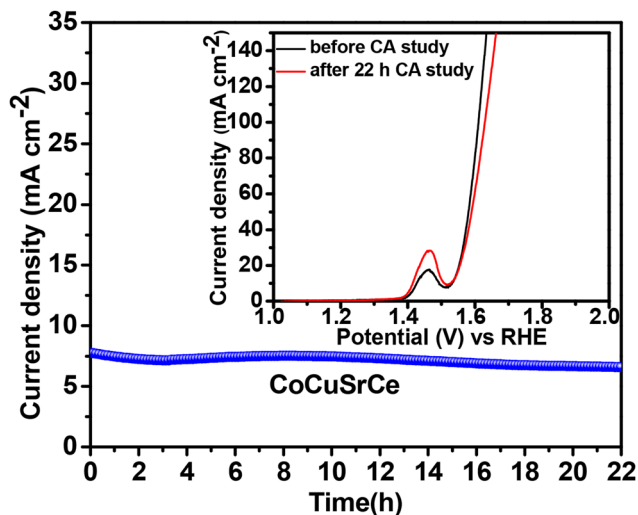


Fig. 7 Chronoamperometry plots of the three synthesized catalysts. The inset shows the polarisation curves of CoCuSrCe before and after the 22 h chronoamperometry study.

The core-level deconvoluted Ce 3d XPS spectra of the exhausted catalysts are shown in Fig. 8b. The spectra reveal the same 5 spin-orbit coupled peaks corresponding to the  $\text{Ce}^{4+}$  and  $\text{Ce}^{3+}$  oxidation states as the fresh catalyst (Fig. 4a). However, after OER, the concentration of  $\text{Ce}^{4+}$  in the exhausted

catalysts reduced to 61.3, 58.6 and 51% for CoCe, CoSrCe and CoCuSrCe, respectively. Notably, 65.6, 68.0 and 74.1% of  $\text{Ce}^{4+}$  were present in the as-prepared CoCe, CoSrCe and CoCuSrCe catalysts, respectively. This signifies the highly reducible nature of  $\text{Ce}^{4+}$  in these catalysts and that the extent of reduction of  $\text{Ce}^{4+} \rightarrow \text{Ce}^{3+}$  during the positive potential sweep of OER must occur alongside parallel oxidation reactions. These parallel oxidation reactions can be attributed to the oxidation of  $\text{Co}^{2+} \rightarrow \text{Co}^{3+}$  and/or the evolution of lattice oxygen ( $\text{O}^{2-} \rightarrow \frac{1}{2}\text{O}_2 + 2\text{e}^-$ ) to create oxygen vacancies. Therefore, either the  $\text{Co}^{3+}$  ions or the adjacent oxygen vacancies are responsible for the formation of the  $-\text{OOH}$  species, which was also observed evidently in the XRD pattern of the exhausted catalyst. To corroborate this hypothesis, we collected the core-level Co 2p spectra of the exhausted catalysts (Fig. 8c). Interestingly, the relative ratios of  $\text{Co}^{3+}/\text{Co}^{2+}$  increased to 66.5, 75.2, and 79.1% in CoCe, CoSrCe and CoCuSrCe, respectively. We further probed the O 1s spectra, and the deconvoluted spectrum is plotted in Fig. 8d. The extra peak at 535 eV is attributed to the intermediate  $-\text{OOH}$  formed during the OER. The corresponding peak, however, could be attributed to the generation of  $\text{Co}-\text{OOH}$  and/or  $\text{Cu}-\text{OOH}$ . The surface  $\text{O}_\text{L}$  content (%) was found to be significantly reduced to 7.9% after the OER reaction. The comprehensive structural and surface study revealed that the facile reduction of  $\text{Ce}^{4+} \rightarrow \text{Ce}^{3+}$

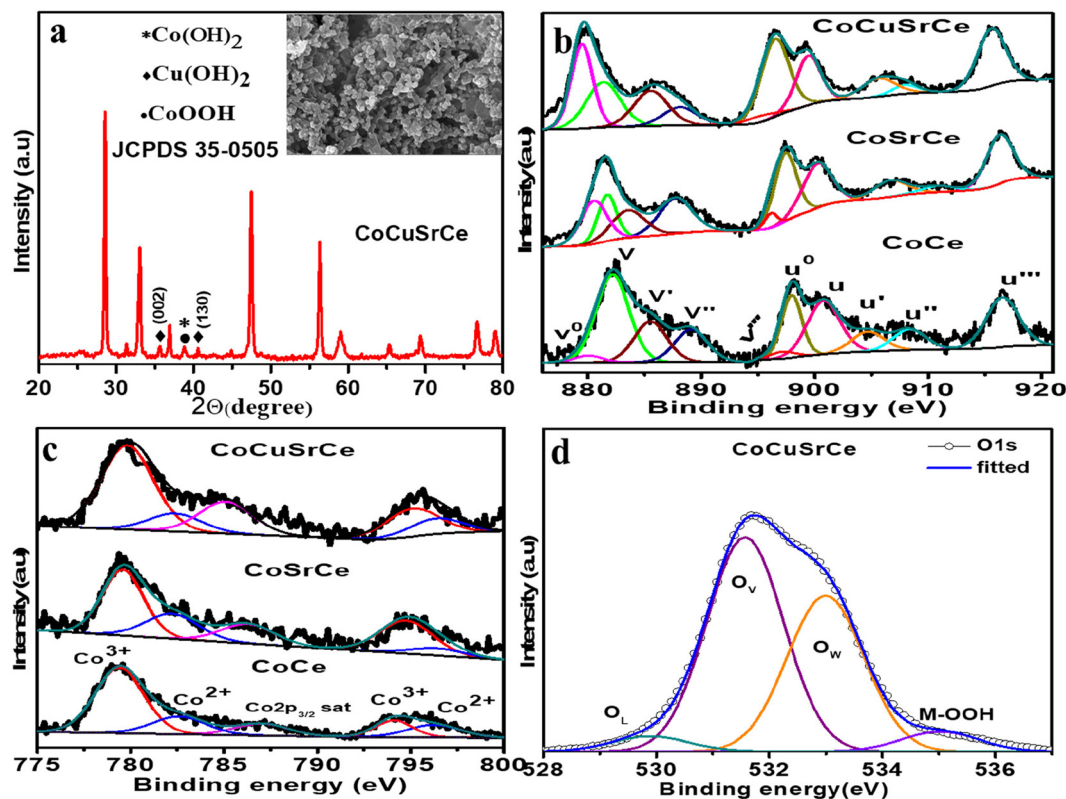


Fig. 8 (a) XRD pattern of CoCuSrCe and its FESEM image in the inset; the core level (b) Ce 3d (c) Co 2p spectra of all three exhausted composite oxides after 12 h of chronoamperometry OER; (d) O 1s of exhausted CoCuSrCe after the 12 h chronoamperometry study.



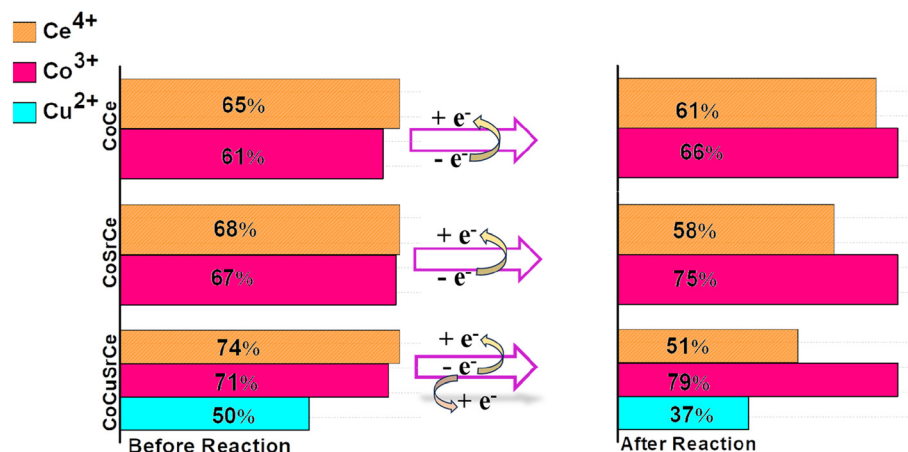


Fig. 9 Change in the content (%) of Ce<sup>4+</sup>, Co<sup>3+</sup> and Cu<sup>2+</sup> during the OER over the three catalysts.

during the positive potential of OER helped the parallel occurrence of both oxidation of Co<sup>2+</sup> → Co<sup>3+</sup> and the evolution of lattice oxygen to create oxygen vacancies primarily on the surface of the oxides, and the extent of reduction of Ce<sup>4+</sup> along with the oxidation of Co<sup>3+</sup> was found to be the maximum in CoCuSrCe (Fig. 9). The formation of Co<sup>3+</sup> along with oxygen vacancies due to the electronic interaction of the catalyst with the support helped the formation of the key intermediate –OOH, which in turn reduced the activation energy barrier and thereby enhanced the kinetics of oxygen evolution over the CoCuSrCe catalyst. However, in addition to Co<sup>3+</sup>, the presence of Cu<sup>2+</sup> on the surface of CoCuSrCe also accelerated the OER efficacy, as observed from the XRD pattern and the core level O 1s XPS.

and facile progression of the oxygen evolution reaction. In addition to Co<sup>3+</sup>, the presence of Cu<sup>2+</sup> on the surface of CoCuSrCe might also accelerate the OER kinetics, as evidenced by the XRD pattern and XPS spectrum of the exhausted catalyst. Overall, these findings underscore the significance of the electronic interactions between the active catalytic sites and the support, as well as the involvement of oxygen vacancies, in realizing sustainable advancement of the H<sub>2</sub> economy in the future.

## Conflicts of interest

There are no conflicts to declare.

## Acknowledgements

Authors thank BITS Pilani Hyderabad Campus for the financial support.

## References

- 1 L. C. Seitz, C. F. Dickens, K. Nishio, Y. Hikita, J. Montoya, A. Doyle, C. Kirk, A. Vojvodic, H. Y. Hwang, J. K. Nørskov and T. F. Jaramillo, *Science*, 2016, **353**, 1011–1014.
- 2 T. Reier, H. N. Nong, D. Teschner, R. Schlögl and P. Strasser, *Adv. Eng. Mater.*, 2017, **7**, 1601275.
- 3 I. Roger, M. A. Shipman and M. D. Symes, *Nat. Rev. Chem.*, 2017, **1**, 0003.
- 4 Y. Yan, B. Y. Xia, B. Zhao and X. Wang, *J. Mater. Chem. A*, 2016, **4**, 17587–17603.
- 5 P. C. Meenu, S. Roy, C. Chakraborty and S. Roy, *Adv Powder Technol*, 2021, **32**, 2663–2689.
- 6 A. Adruzaman, A. Yuda, A. Ashok and A. Kumar, *Inorg. Chim. Acta*, 2020, **511**, 119854.
- 7 Y. Li, F. M. Li, X. Y. Meng, S. N. Li, J. H. Zeng and Y. Chen, *ACS Catal.*, 2018, **8**, 1913–1920.

## 4. Conclusion

The three composite catalysts were synthesized by a single-step solution combustion route. The Rietveld refinement of the powder XRD pattern of CoCe revealed the co-existence of Co<sub>3</sub>O<sub>4</sub>/CeO<sub>2</sub>. Similarly, CoSrCe showed the presence of Co<sub>3</sub>O<sub>4</sub>/Ce<sub>0.9</sub>Sr<sub>0.1</sub>O<sub>2-δ</sub> and CoCuSrCe was composed of Co<sub>3-x</sub>Cu<sub>x</sub>O<sub>4</sub>, Ce<sub>0.9</sub>Sr<sub>0.1</sub>O<sub>2-δ</sub>, SrCoO<sub>2.8</sub> and CuO. The electrochemical surface area of doped CoCuSrCe was found to be 3 times higher than that of CoCe. In the electrocatalytic OER studies, the doped material CoCuSrCe outperformed the other two composites, showing the highest current density and highest faradaic efficiency at the lowest overpotential. CoCuSrCe also exhibited the lowest Tafel slope of 42 mV dec<sup>-1</sup> and the lowest OER activation energy of 11.7 kJ mol<sup>-1</sup>. The outstanding stability of the catalyst CoCuSrCe was observed in the 12 h OER study at a considerably strong alkaline condition. The detailed mechanistic studies indicate that the favourable reducibility of cerium introduces a higher concentration of Co<sup>3+</sup> ions at the catalytic sites, leading to enhanced formation of the Co–OOH species. Further, the lower-valence Sr and Cu ions doped at the Ce and Co sites, respectively, accelerate the formation of the active Co<sup>3+</sup> species, as well as oxygen vacancies, aiding the efficient



- 8 T. Y. Ma, S. Dai, M. Jaroniec and S. Z. Qiao, *J. Am. Chem. Soc.*, 2014, **136**, 13925–13931.
- 9 M. Li and L. Feng, *Chin. J. Struct. Chem.*, 2022, **41**, 2201019–2201024.
- 10 F. G. Wang, X. Liu, Q. X. Lv, B. Liu, Y. M. Chai and B. Dong, *Chin. J. Struct. Chem.*, 2022, **41**, 2209008–2209044.
- 11 J. Qi, W. Zhang and R. Cao, *Chem. Commun.*, 2017, **53**, 9277–9280.
- 12 A. Moysiadou, S. Lee, C. S. Hsu, H. M. Chen and X. Hu, *J. Am. Chem. Soc.*, 2020, **142**, 11901–11914.
- 13 S. Roy, N. Devaraj, K. Tarafder, C. Chakraborty and S. Roy, *New J. Chem.*, 2022, **46**, 6539–6548.
- 14 Y. Liu, C. Ma, Q. Zhang, W. Wang, P. Pan, L. Gu, D. Xu, J. Bao and Z. Dai, *Adv. Mater.*, 2019, **31**, 1900062.
- 15 J. X. Feng, S. H. Ye, H. Xu, Y. X. Tong and G. R. Li, *Adv. Mater.*, 2016, **28**, 4698–4703.
- 16 F. Esch, S. Fabris, L. Zhou, T. Montini, C. Africh, P. Fornasiero, G. Comelli and R. Rosei, *Science*, 2005, **309**, 752–755.
- 17 J. H. Kim, K. Shin, K. Kawashima, D. H. Youn, J. Lin, T. E. Hong, Y. Liu, B. R. Wygant, J. Wang, G. Henkelman and C. B. Mullins, *ACS Catal.*, 2018, **8**, 4257–4265.
- 18 P. C. Meenu and S. Roy, *ACS Appl. Energy Mater.*, 2023, **6**, 11212–11225.
- 19 P. C. Meenu and S. Roy, *ACS Appl. Mater. Interfaces*, 2023, **15**, 36154–36166.
- 20 J. Kim, P. C. Shih, K. C. Tsao, Y. T. Pan, X. Yin and C. J. Sun, *J. Am. Chem. Soc.*, 2017, **139**, 12076–12083.
- 21 K. Sardar, S. C. Ball, J. D. B. Sharman, D. Thompsett, J. M. Fisher, R. A. P. Smith, P. K. Biswas, M. R. Lees, R. J. Kashtiban, J. Sloan and R. I. Walton, *Chem. Mater.*, 2012, **24**, 4192–4200.
- 22 J. Park, M. Park, G. Nam, M. G. Kim and J. Cho, *Nano Lett.*, 2017, **17**, 3974–3981.
- 23 J. B. Goodenough, R. Manoharan and M. Paranthaman, *J. Am. Chem. Soc.*, 1990, **112**, 2076–2082.
- 24 P. Bothra and S. K. Pati, *ACS Energy Lett.*, 2016, **1**, 858–862.
- 25 Q. Wang, X. Xue, Y. Lei, Y. Wang, Y. Feng, X. Xiong, D. Wang and Y. Li, *Small*, 2020, **16**, 2001571.
- 26 Y. Zheng, S. Chen, K. A. I. Zhang, J. Zhu, J. Xu, C. Zhang and T. Liu, *ACS Appl. Mater. Interfaces*, 2021, **13**, 13328–13337.
- 27 X. Jiang, Y. Dong, Z. Zhang, J. Li, J. Qian and D. Gao, *J. Alloys Compd.*, 2021, **878**, 160433.
- 28 A. Valipour, N. Hamnabard, S. M. H. Meshkati, M. Pakan and Y. H. Ahn, *Dalton Trans.*, 2019, **48**, 5429–5443.
- 29 J. H. Scofield and J. Electron, *Spectrosc. Relat. Phenom.*, 1976, **8**, 129–137.
- 30 R. Rameshan, P. Pentyla, S. A. Singh, P. A. Deshpande and S. Roy, *J. Environ. Chem. Eng.*, 2022, **10**, 108966.
- 31 S. Payra and S. Roy, *J. Phys. Chem. C*, 2021, **125**, 8497–8507.
- 32 T. Baidya, T. Mazumder, K. Y. Koltunov, P. R. Likhar, A. H. Clark, K. Tiwari, V. I. Sobolev, S. Payra, T. Murayama, M. Lin, P. Bera, S. Roy, K. Biswas, O. Safonova, B. Srinivasa Rao and M. Haruta, *J. Phys. Chem. C*, 2020, **124**, 14131–14146.
- 33 C. Wang, L. Zeng, W. Guo, C. Gong and J. Yang, *RSC Adv.*, 2019, **9**, 35646–35654.
- 34 M. A. Khan, N. Nayan, Shadiullah, M. K. Ahmad and C. F. Soon, *Nanomaterials*, 2020, **10**, 1298.
- 35 S. Payra, S. Kanungo and S. Roy, *Nanoscale*, 2022, **14**, 13352–13361.
- 36 S. Payra, N. Devaraj, K. Tarafder and S. Roy, *ACS Appl. Energy Mater.*, 2022, **5**, 4945–4955.
- 37 V. S. Kirankumar and S. Sumathi, *J. Mater. Sci.: Mater. Electron.*, 2018, **29**, 8738–8746.
- 38 S. K. Shinde, D. P. Dubal, G. S. Ghodake and V. J. Fulari, *RSC Adv.*, 2015, **5**, 4443–4447.
- 39 F. C. de Godoi, E. Rodriguez-Castellon, E. Guibal and M. M. Beppu, *Chem. Eng. J.*, 2013, **234**, 423–429.
- 40 A. Hezam, K. Namratha, Q. A. Drmash, D. Ponnammam, J. Wang, S. Prasad, M. Ahamed, C. Cheng and K. Byrappa, *ACS Appl. Nano Mater.*, 2020, **3**, 138–148.
- 41 T. Ye, W. Huang, L. Zeng, M. Li and J. Shi, *Appl. Catal., B*, 2017, **210**, 141–148.
- 42 D. Jiang, W. Wang, L. Zhang, Y. Zheng and Z. Wang, *ACS Catal.*, 2015, **5**, 4851–4858.
- 43 S. Payra, S. K. Ganeshan, S. Challagulla and S. Roy, *Adv. Powder Technol.*, 2020, **31**, 510–520.
- 44 A. K. Venugopal, A. T. Venugopalan, P. Kaliyappan and T. Raja, *Green Chem.*, 2013, **15**, 3259–3267.
- 45 C. W. Tang, C. B. Wang and S. H. Chien, *Thermochim. Acta*, 2008, **473**, 68–73.
- 46 A. Mehboob, S. R. Gilani, A. Anwar, A. Sadiqa, S. Akbar and J. Patujo, *J. Appl. Electrochem.*, 2021, **51**, 691–702.
- 47 S. Sun, H. Li and Z. J. Xu, *Joule*, 2018, **2**, 1024–1027.
- 48 T. Y. Ma, S. Dai, M. Jaroniec and S. Z. Qiao, *J. Am. Chem. Soc.*, 2014, **136**, 13925–13931.
- 49 H. Y. Wang, S. F. Hung, H. Y. Chen, T. S. Chan, H. M. Chen and B. Liu, *J. Am. Chem. Soc.*, 2016, **138**, 36–39.
- 50 X. Xiao, C. T. He, S. Zhao, J. Li, W. Lin, Z. Yuan, Q. Zhang, S. Wang, L. Dai and D. Yu, *Energy Environ. Sci.*, 2017, **10**, 893–899.
- 51 C. Alex, S. C. Sarma, S. C. Peter and N. S. John, *ACS Appl. Energy Mater.*, 2020, **3**, 5439–5447.
- 52 T. Maiyalagan, K. A. Jarvis, S. Therese, P. J. Ferreira and A. Manthiram, *Nat. Commun.*, 2014, **5**, 3949.
- 53 Z. Zhao, M. Yu, Y. Liu, T. Zeng, R. Ye, Y. Liu, J. Hu and A. Li, *Adv. Energy Sustainability Res.*, 2023, **4**, 2300123.
- 54 P. C. Meenu, P. K. Samanta, T. Yoshida, N. J. English, S. P. Datta, S. A. Singh, S. Dinda, C. Chakraborty and S. Roy, *ACS Appl. Energy Mater.*, 2022, **5**, 503–515.
- 55 Q. Xu, H. Jiang, H. Zhang, H. Jiang and C. Li, *Electrochim. Acta*, 2018, **259**, 962–967.
- 56 Y. Xiao, Y. Wang, M. Xiao, C. Liu, S. Hou, J. Ge and W. Xing, *NPG Asia Mater.*, 2020, **12**, 73.
- 57 Y. Si, C. Guo, C. Xie and Z. Xiong, *Materials*, 2018, **11**, 1912.
- 58 Z. Zhai, Y. You, L. Ma, D. Jiang, F. Li, H. Yuan, M. Zheng and W. Shen, *Nanoscale Res. Lett.*, 2019, **14**, 167.
- 59 S. Song, H. Bao, X. Lin, X. L. Du, J. Zhou, L. Zhang, N. Chen, J. Hu and J. Q. Wang, *J. Energy Chem.*, 2020, **42**, 5–10.

